

CHARACTERIZATION OF A 5kW-CLASS HALL THRUSTER VIA 2D HYBRID SIMULATIONS

ESTORIL, PORTUGAL / 17 – 19 MARCH 2021

J. Perales-Díaz¹, A. Domínguez-Vázquez¹, P. Fajardo¹, E. Ahedo¹, F. Faraji², M. Reza², T. Andreussi²

¹Equipo de Propulsión Espacial y Plasmas, EP2, Universidad Carlos III de Madrid, Leganés, Spain.

Email: jperales@ing.uc3m.es

²SITAE S.p.A., Via A. Gherardesca 5, 56121 Pisa, Italy,

Email: tommaso.andreussi@sitael.com

KEYWORDS: Hall effect thrusters, particle-in-cell simulations, Direct-Drive, turbulent transport, magnetic shielding

ABSTRACT:

Numerical simulations of SITAE HT5k magnetically-shielded Hall effect thruster are performed with HYPHEN, a two-dimensional axisymmetric hybrid PIC/fluid code featuring a diffusive magnetized electron transport model. A physically sound fully 2D characterization of the plasma discharge both in the thruster chamber and the near plume region is presented. The magnetic shielding yields low electron temperature near the thruster chamber walls, which is beneficial from the point of view of erosion of the walls. A phenomenological turbulent transport model is adjusted to fit experimental data. The turbulent parameters of the model vary mildly along the different operation points with a linear dependence on the power source voltage. Performance figures are in good agreement with the experimental data in a certain range of operation. Power and current balances, along with relevant efficiencies, are computed and analyzed.

1 INTRODUCTION

EDDA (European Direct-Drive Architecture) is an EU-funded H2020 project aiming at increasing the power chain efficiency of an electrical propulsion (EP) based spacecraft through an innovative architecture that enables the direct feeding of the electric thrusters with solar electric power without intermediate power conversion. This innovation may lead to important savings in volume and costs for multiple applications, including telecommunications and space-tug satellites, associated with the removal of power converters and the subsequent decrease of thermal dissipation.

One of the thruster technologies considered for the Direct-Drive concept is the Hall effect thruster (HET). In particular, the HT5k thruster, an advanced magnetically-shielded HET developed by SITAE

[1, 2], is chosen to be embedded within this architecture. The design and development of the Direct-Drive architecture requires a precise characterization of the thruster performance and electrical characteristics. Particularly, the determination of the thruster I-V curve in the nominal operation range is crucial for the correct integration of the thruster with other subsystems of the direct drive concept, including the power bus management and fluidic subsystems.

In order to accomplish this, a test campaign and a numerical simulation study of the HT5k are carried out within the framework of the EDDA project. Regarding the latter, the advanced two-dimensional axisymmetric hybrid simulation code HYPHEN (standing for HYbrid Plasma thruster Holistic simulation ENvironment) is used [3, 4]. HYPHEN uses a particle-in-cell (PIC) formulation for heavy species and a fluid one for electrons. The HET version of HYPHEN, developed by the EP2 group at UC3M in the frame of the CHEOPS H2020 project, has been successfully adapted to the simulation of magnetically-shielded HETs such as the HT5k, featuring complex magnetic topologies including singular magnetic points, in the context of the EDDA project.

This paper describes a part of the numerical simulation activities and results developed for the HT5k thruster in the context of the EDDA project. In particular, the adjustment of the phenomenological turbulent transport model to fit some experimental data provided by SITAE, is presented. The experimentally reported enhanced axial electron transport in HETs [5, 6], not predicted by classical theory, is still one of the main open problems in HET research. HYPHEN incorporates a diffusive-collisional approach for modelling this electron ‘anomalous’ transport [3, 4]. Although this approach cannot help in the understanding of the physical mechanisms behind this phenomenon, it permits a validation of the simulation model against experiments through an experimental data-driven tuning of several model parameters. A fully 2D description of relevant plasma properties is presented and analyzed, showing, among other things, the ef-

fect of the magnetic shielding on the plasma behavior inside the chamber. A comparison to the experimental data in terms of main thruster performance figures and I-V curve is presented, along with the analysis of current and power balances for several operation points within the nominal range for EDDA project purposes.

The rest of the manuscript is structured as follows. Section 2 presents a brief description of the simulation model. Then, the thruster unit is introduced in Section 3. The simulation set-up is described in Section 4. Section 5 contains the simulation results and their comparison to the experimental data. Finally, the conclusions are drawn in Section 6.

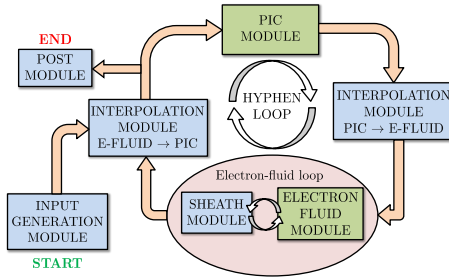


Figure 1: HYPHEN loop schematics.

2 MODEL

HYPHEN is a two-dimensional (axisymmetric) hybrid, OpenMP parallelized multi-thruster simulation code built modularly for HET simulations. The code consists of three main modules: the ion (PIC) module, which follows a Lagrangian approach for simulating the dynamics of the macroparticles representing the heavy species (i.e. ions and neutrals); the electron module, that considers a magnetized fluid model for the electrons; and a sheath module that provides the proper coupling between the quasineutral plasma and the thruster walls by solving the non-neutral plasma sheaths that develop around the walls; these are treated as surface discontinuities by the quasineutral plasma simulator. The main features of each module are detailed in [3, 4, 7–10]. Here the simulation loop is briefly outlined. Every simulation step, the ion module takes as inputs the externally applied magnetic field B , the electric potential ϕ and the electron temperature T_e , and performs the injection, collisions and propagation of the heavy species one simulation timestep forward, computing the plasma production through the ionization of the injected neutral gas and obtaining, for each heavy species s , the particle density n_s and particle flux g_s through a particle-to-mesh weighting process. The electron module, taking those values from the ion module and considering quasineutrality (i.e. $n_e = \sum_{s \neq e} Z_s n_s$, with Z_s the charge number of the species s), solves a fluid model of the electron population computing the electric potential, the elec-

tron temperature, the electron current density vector j_e and the electron heat flux vector q_e . The electron turbulent transport model defines an electron collisionality as a fraction of the electron gyrofrequency, $\nu_t = \alpha_t \omega_{ce}$, being $\omega_{ce} = eB/m_e$ the electron gyrofrequency with e and m_e the electron charge and elementary mass, and α_t a non-dimensional turbulent parameter (refer to [3, 4] for further details). The ion and the electron modules operate on a different mesh of the simulation domain: a structured mesh for the former (referred to as the PIC mesh hereafter), and an unstructured magnetic field aligned mesh (MFAM) for the latter. A schematic representation of the simulation step in HYPHEN is shown in Fig. 1.

3 THRUSTER UNIT

In 2013, SITAEL started the development of the HT5k-TU (in Fig. 2), a 5 kW-class thruster unit composed of two main elements, the HT5k Hall thruster and the HC20 hollow cathode. In the past years, three different development models (DMs) of the HT5k were designed, manufactured, and tested, as part of several national and international programmes. The thruster unit prototypes passed through several technical investigations [2, 11], which allowed to demonstrate high performance, low erosion, direct-drive operations, as well as performance stability in high-vacuum conditions (pressure $< 1E-5$ mbar). Design and manufacturing of the HT5k TU engineering qualification model started in 2019, when the thruster unit was selected as the main propulsive unit for the orbit raising and station keeping of the Ital-GovSatCom geostationary platform [12]. The HT5k-TU EQM will be tested extensively during the first half of 2021, in order to pave the way for the qualification of the thruster unit. In Sec. 5.1, experimental results of the HT5k DM3 are presented. This prototype implements the main features of the HT5k-TU, i.e. a centrally mounted cathode and a non-conventional magnetic field topology, which allows for a significant reduction of the discharge channel erosion. Design and testing efforts were dedicated to improve critical components and to optimize the thruster thermal behaviour. The thruster testing took place in SITAEL's IV10 facility, achieving pressures of the order of $7E-6$ mbar (Xe) while firing a 4.4 kW of discharge power. The HT5k-TU DM3 showed competitive performance and demonstrated stable and efficient operation in the 3 kW to 7 kW discharge power range, achieving anodic efficiencies up to 60%.

4 SIMULATION SET-UP

Figs. 3(a) and 3(b) show the PIC mesh and the MFAM of the HT5k simulation domain. Both meshes

have been refined and optimized to reduce discretization and interpolation errors, while keeping a reasonable simulation time. These figures also show the geometry of the thruster chamber, the injection surface, the anode and cathode keeper surfaces, and the plume region included in the simulation domain. The main features of these meshes are listed in Tab. 1, along with some other relevant simulation parameters. The cathode is represented by a MFAM element at which $\phi = 0$, whose location is indicated by the black square marker in Fig. 3(b). The discharge current I_d collected at the anode wall (green boundary in Fig. 3(a)) is injected into the domain through the cathode by performing an electron thermal emission at a temperature of 3 eV for all cases simulated. Also in Fig. 3(a), one can identify the rest of boundaries: in red, the material dielectric walls; in blue, the free loss boundaries; and, in magenta, the symmetry axis. The way in which these boundaries are modeled is detailed in [4].

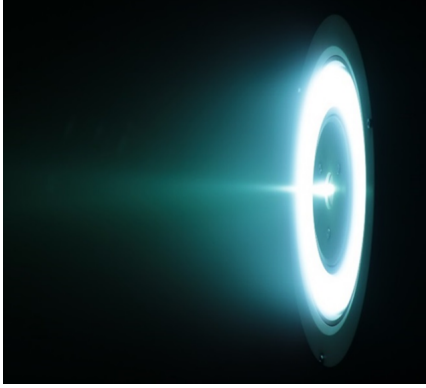


Figure 2: HT5k-TU-DM3.

In Tab. 1, one can find the SEE (Secondary Electron Emission) crossover energy for dielectric walls, E_c , and the emission temperature of SEE. Fig. 3(d) sketches the RLC filter connecting anode and cathode and the discharge voltage and current, V_d and I_d . The values of the RLC filter elements are $R = 4.7 \Omega$, $L = 360 \mu\text{H}$, and $C = 94 \mu\text{F}$. Although the purpose of the RLC filter is that of protecting other parts of the satellite's electric circuit, not the thruster, it is included in the simulations to study its effect on the discharge. Indeed, this device filters the simulation input V_s , the power source voltage, to V_d . Also in Fig. 3(d), we see the position of the hollow cathode in the center line of the thruster.

The simulations with HYPHEN require to be verified with experimental data, in order to tune parameters related to those physical phenomena which (a) remain without a well established theoretical frame or (b) depend on details of the electron velocity distribution function (VDF) beyond the scope of an electron fluid model. The main phenomenon requiring parameter tuning is, in the present work, the turbulent transport. Its treatment in HYPHEN involve several parameters, but only the main one is analyzed

here.

This key parameter is the coefficient α_t , which represents the anomalous momentum transport. It allows one to include a Bohm-like diffusivity on the electron momentum equations. This parameter, of the order of 10^{-2} , will be defined with an axial step-out profile [4, 13–18], as shown in Fig. 3(c), and the initial and final values of the step are to be tuned using the available experimental results.

Table 1: Main simulation parameters and mesh characteristics. The values of the power voltage source and the anode mass flow are specific of the reference operation point.

Simulation parameter	Units	Value
PIC mesh number of cells, nodes	-	2582, 2696
MFAM number of cells, faces	-	2735, 5599
V_s , ref. case	V	300
\dot{m}_A , ref. case	mg/s	14
Simulation (PIC) timestep, Δt	s	$1.50 \cdot 10^{-8}$
Total number of simulation steps	-	60000
Injected Xe velocity (sonic)	ms^{-1}	300
Injected Xe temperature	eV	$7.35 \cdot 10^{-2}$
Injected Xe mass flow, \dot{m}_A	mgs^{-1}	14
SEE crossover energy, E_c	eV	50
SEE temperature, dielectric walls	eV	2

Table 2: All experimental data. The data repeatability for the measurements of I_d at each point of operation is $\pm 5\%$. Bold letters highlight the five cases for the turbulent parameters tuning. The reference operation point is $\dot{m}_A, V_s = (14 \text{mg/s}, 300 \text{V})$

\dot{m}_A (mg/s)	V_s (V)	I_d (A)	F (mN)	I_{sp} (s)
8	300	8.2	-	-
8	350	8.1	-	-
8	400	8.4	-	-
8	450	8.9	-	-
10	250	10.8	-	-
10	300	10.3	184	1876
10	350	10.1	197	2008
10	400	9.6	208	2120
10	450	10.3	-	-
14	250	15.5	-	-
14	300	14.6	269	1959
14	350	15.5	-	-
14	400	14.2	308	2243
14	450	13.9	-	-

5 RESULTS

Firstly, the experimental data of the HT5k thruster provided by SITAEL are presented, in Sec. 5.1. Then, the results from the simulations with HYPHEN

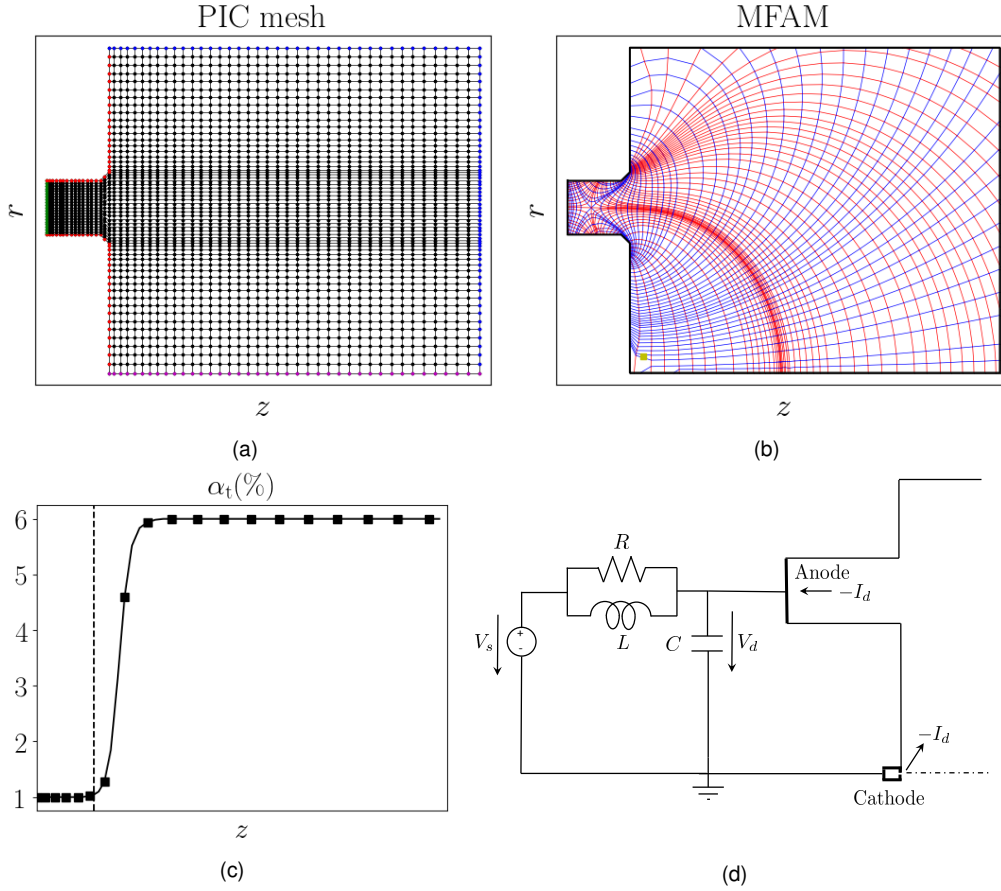


Figure 3: (a) The PIC mesh used by the PIC module for the simulation of the heavy species (ions and neutrals). The red, green, blue and magenta lines indicate the thruster dielectric walls, the anode wall, the free loss boundary and the symmetry axis at $r = 0$, respectively. (b) The MFAM used by the electron-fluid module. The blue and red MFAM faces defining the MFAM cells are aligned along the magnetic field parallel and perpendicular directions, respectively. The yellow square indicates the position of the volumetric cathode considered for the simulations, whose coordinates are listed in Tab. 1. (c) Step-out profile of the electron turbulence parameter, α_t , along the thruster chamber center line. The dashed vertical line indicates the axial position of the channel exit plane. (d) Scheme of the RLC filter unit implemented between the thruster anode wall and the cathode keeper.

of the same thruster are shown and compared to the experimental measurements in Secs. 5.2 and 5.3. In particular, in Sec. 5.2, the reference operation point simulation results are discussed in detail, and in Sec. 5.3 an I-V curve obtained from the simulations is presented, and compared and improved with the input experimental data introduced in Sec. 5.1. In Sec. 5.4, power and current balances and important efficiencies are shown and commented for several operation points.

5.1 Experimental data

In Tab. 2, the main experimental data of the HT5k prototype are gathered. They mainly consist of measurements of time averaged performance metrics, namely the discharge current, I_d , and the thrust, F , for a certain range of operational points defined by a certain anodic mass flow rate, \dot{m}_A , and voltage of the power source, V_s . The former ranges from 8

mg/s to 14 mg/s, while the latter, from 250 V to 450 V. This same range of operational points is considered in the simulation studies.

5.2 Reference point results

As indicated in Tab.1, the reference operation point for the simulations is chosen to be $\dot{m}_A, V_s = (14\text{mg/s}, 300\text{V})$, because it is the point for which more experimental data are available, which are needed for the adequate tuning of α_t . Notice that the tuning process is based on the matching between the time-averaged performance figures of the simulation and the experiments. During this process, the two values of the in-out step profile of α_t (α_{t1} being the upstream value and α_{t2} the downstream one) were varied until a certain proximity with the experimental performance metrics was achieved (defined as a relative difference smaller than a 5% in I_d and F , below the standard devia-

tion of the experimental data in Tab. 2). The second row in Tab. 3 shows the result of the tuning process. In the first row, the experimental measurements for the reference operation point are shown again for the sake of comparison. In the last column of Tab. 3, the values of the thrust efficiency are presented. Its definition is:

$$\eta = \frac{F^2}{2\dot{m}_A P_d} \quad (\text{Eq. 1})$$

One can see that both values of the efficiency are similar, as it occurs with the values of the frequency of the discharge current oscillations, f_d .

It is also worth mentioning that, once the tuning process for the reference operation point was finished, the influence of the RLC filter on the plasma discharge was tested and was proved to be negligible. With the turbulent parameters tuned, the reference point simulation yields the contour plots in Figs. 4 and 5. They depict time-averaged contour scalar and vectorial fields, over the whole simulation domain (right column) or inside the chamber (left column), of plasma properties of relevance for the analysis of the discharge of the HT5k. The electric potential, Fig. 4 (a), exhibits a rather constant value inside the chamber, with a maximum somewhere in the middle of it. Then, at the chamber exit, as seen in Fig. 4(b), it steeply falls towards the cathode and its magnetic line (the magnetic line that goes through the cathode), effectively accelerating the ions downstream. The contour lines of ϕ outside the chamber seem to closely follow the magnetic lines. This is due to the relatively high mobility that the magnetized electrons have along the magnetic lines, which tend to reduce any potential gradient along these lines. It occurs similarly in the case of the electron temperature, in Figs. 4(g) and 4(h); with the difference that T_e also follows the magnetic lines inside the chamber, yielding low T_e at the chamber walls, which is beneficial from the point of view of erosion. Moreover, regarding the electron temperature, its maximum value is reached at the exit plane of the thruster, where the electrons from the cathode converge to come into the chamber and, at the same time, find their mobility towards the anode reduced by the perpendicular magnetic field. The fact that, inside the chamber and near its exit, the electric potential lines are not parallel to B is due to the pressure gradient along the magnetic field lines, induced by the plasma density distribution governed by ion dynamics, which is compensated by an electric potential gradient parallel to B . In Figs. 4(c) and 4(d), the neutral density contour provides information about the ionization along the domain. The neutrals are injected through the anode surface and, already inside the chamber, their density value falls about 2 orders of magnitude, indicating that a significant amount of ionization takes place. This seems to mainly occur near the exit plane, where the temperature is higher. This position of the main ioniza-

tion region may have a positive impact on erosion reduction. The electron density, n_e , in Fig. 4(f), is higher inside the chamber where part of the electrons emitted by the cathode have ionized the neutral gas and are slowed down by the magnetic field on their way to the anode. In Fig. 4(e), one can appreciate the peak in electron density, which is found near the center of the thruster channel. This point coincides with the singularity in the magnetic field topology, seen in Fig. 3(b), which forces a great part of the electron current through a narrow cross sectional area on its way to the anode, as seen in Fig. 5(c). This electron stream from the cathode can be distinguished, in Fig. 5(d), from the electrons travelling downstream to neutralize the ion current. This ion current features, as seen in Fig. 5(b), a significant divergence, which starts only right after the chamber exit, where the electric potential lines become nearly parallel to the B lines, with a strong radial gradient. Upstream the chamber exit, as seen before, the electric potential does not follow the magnetic lines and its gradient is purely axial. Also inside the chamber, as seen in Fig. 5(a), it seems that the ion streamlines are born (meaning that $\hat{j}_i = 0$) in the neighbourhood of the magnetic field singularity, near the peak of ϕ , as seen in Fig. 4(a). Finally, in Figs. 5(e) and 5(f), the in-plane electric current is shown. One can see how it travels all the way from the anode to the cathode, being the downwards boundaries current free.

Table 3: The first row are experimental data for $V_s = 300$ V and $\dot{m}_A = 14$ mg/s. The second row shows the simulation results with the selected α_t after the tuning process.

	α_t (%)	I_d (A)	f_d (kHz)	F (mN)	η (%)
Exp.	-	14.6	22.0	269	58.2
Sim.	1-6	15.1	20.0	266	56.0

5.3 Thruster performance and I-V curve analysis

In the present section, the operational map is extended by running simulation of multiple operational points, instead of a single point, in particular the ones in Tab. 2. The objective is to compare the results with the experimental measurements and, at the same time, enhance the model by taking the test data as reference, in a similar way to what was done in Sec. 5.2.

As a first step, the numerically simulated operational map is extended using the turbulent parameters of the reference case. The output of those simulations is condensed in Fig. 6, and seems not to match well the experimental results. The latter exhibits a roughly flat non-monotonic profile in the range of operational points, while the former yields a monotonically increasing curve for all cases. Even

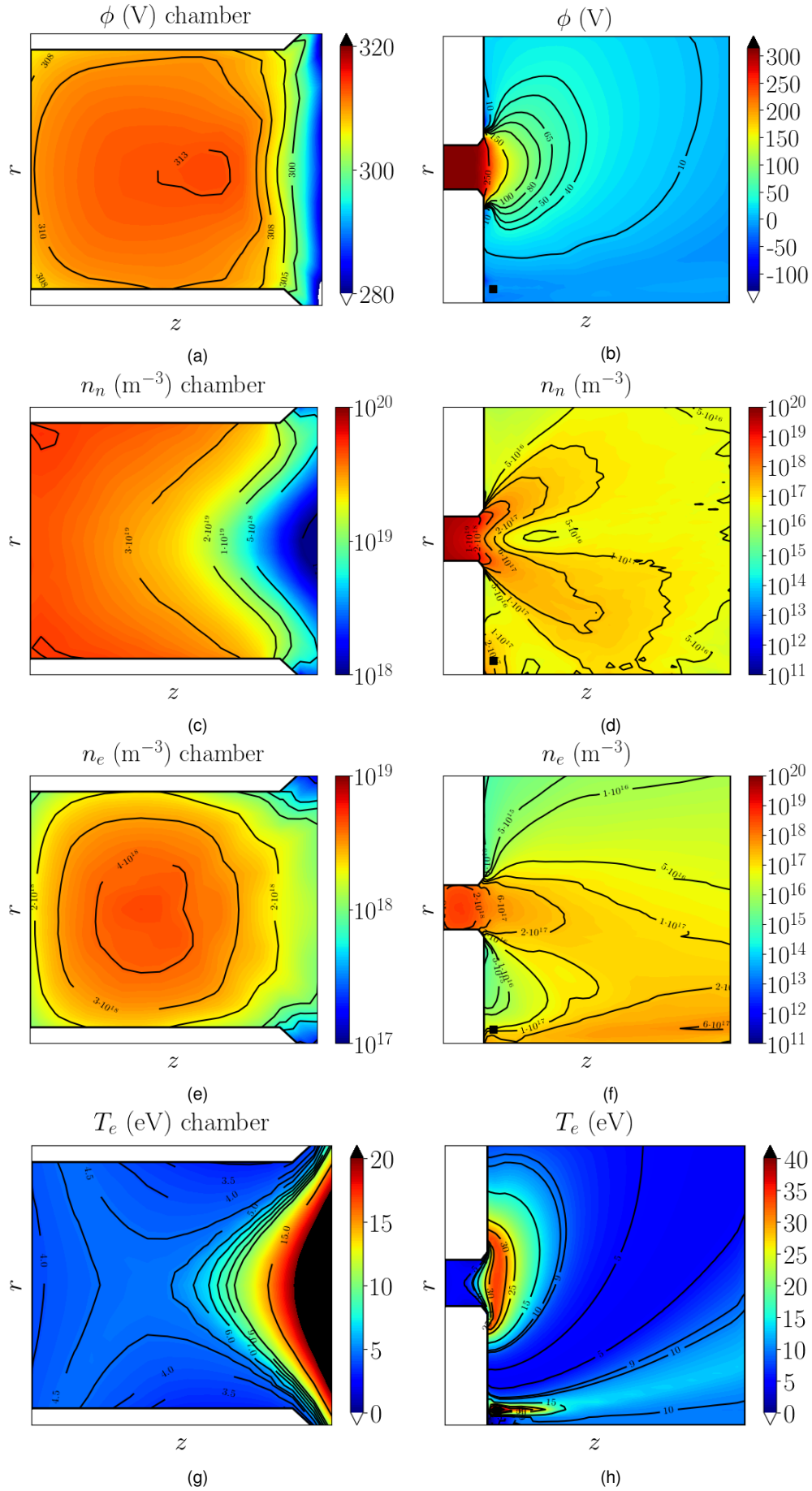


Figure 4: Time-averaged 2D (z,r) contour maps for the reference case, $m_A, V_s=(14 \text{ mg/s}, 300 \text{ V})$. (a)-(b) electric potential, (c)-(d) neutral density, (e)-(f) plasma density, (g)-(h) electron temperature. The black square marker in the right column plots indicates the position of the cathode. Left column plots show detailed contour maps inside the thruster chamber.

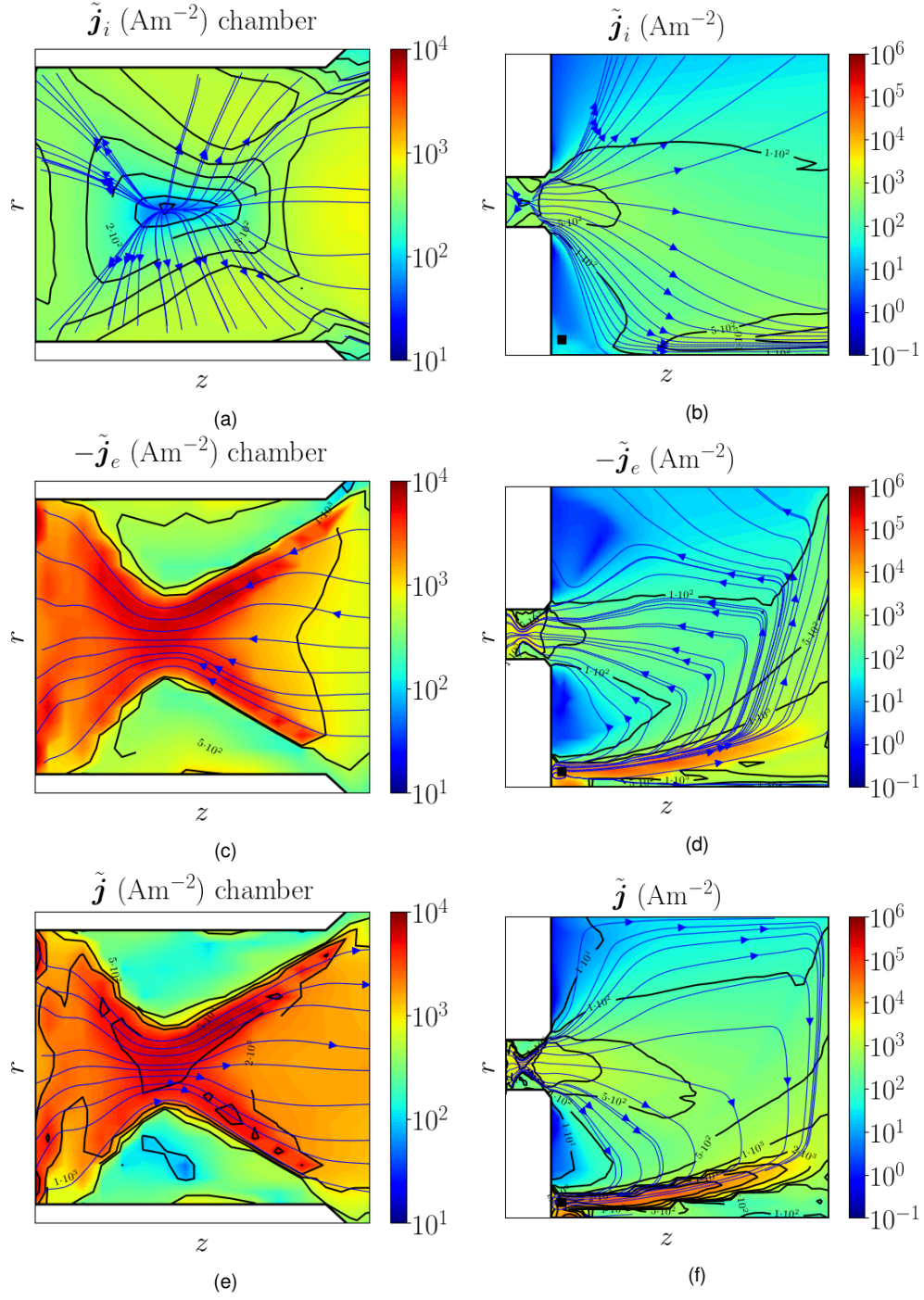


Figure 5: Time-averaged 2D (z,r) contour maps for the reference case, $m_A, V_s=(14 \text{ mg/s}, 300 \text{ V})$. Magnitude of (a)-(b) in-plane ion current density vector \tilde{j}_i , (c)-(d) electron current density vector \tilde{j}_e , (e)-(f) electric current density vector \tilde{j} . Blue lines with arrows depict the \tilde{j}_i , $-\tilde{j}_e$ and \tilde{j} streamlines. The black square marker in the right column plots indicates the position of the cathode. Left column plots show detailed contour maps and streamlines inside the thruster chamber.

in the vicinity of the reference operation point, for which α_t is tuned, the results from experiments and simulations show a relatively large disagreement. This comparison, therefore, seems to indicate that a model in which there exists a dependence of α_t on the operational points, namely on \dot{m}_A and V_s , is better suited for the present problem.

Then, the enhancement of the model consists of matching I_d and F for 5 operational points for which we have such experimental performance data (see Tab. 2), and subsequently obtaining a simple law which relates α_t to V_s and \dot{m}_A . In order to do that, regarding the two values of the step in-out profile, the relations in Tab. 4 were observed. Remember that

α_{t1} corresponds to the upstream value of the profile, while α_{t2} is the downstream one. Then the observed relations have allowed to perform the tuning process whose results are displayed in Tab. 5. In all operation points, the tuning process was carried out until the disagreement between experiments and simulations in the two performance figures is below 5%. Also in Tab. 5, one can see the values of α_{t1} , α_{t2} , for each operation point. With these values a simple linear law is made for each of the two parameters, which are found to be independent, with the available experimental data, of \dot{m}_A . The linear fitting yields the following equations, with $\alpha_{t,i}$ in percentage:

$$\alpha_{t1} = 1.6 - 0.002V_s \quad (\text{Eq. 2})$$

$$\alpha_{t2} = 14.4 - 0.028V_s \quad (\text{Eq. 3})$$

Or, considering the fitting as a linear approximation near point $V_s = V_{s0} = 350 \text{ V}$:

$$\alpha_{t1} = 0.9 - 0.7(V_s - V_{s0})/V_{s0} \quad (\text{Eq. 4})$$

$$\alpha_{t2} = 4.6 - 9.8(V_s - V_{s0})/V_{s0} \quad (\text{Eq. 5})$$

Table 4: Influence of the two different turbulent profile constants on the main performance metrics

	$\alpha_{t1} \uparrow$	$\alpha_{t2} \uparrow$
I_d	\uparrow	\uparrow
F	\downarrow	\uparrow

With this linear fitting, interpolating and extrapolating the values of α_{t1} and α_{t2} to the rest of operational points, the main performance figures are obtained and I_d is shown in Tab. 6. In addition, in Fig. 7, the comparison with experimental results is shown graphically. The simple linear law seems to allow to match acceptably well the experimental results in the range of operational points $V_s = (250-400)\text{V}$ and $\dot{m}_A = (10, 14)\text{mg/s}$. These are the points which are close to the operational points used for the tuning. If, on the contrary, one observes the operational points outside this range, "far" from the points used for the tuning, one can see that the disagreement with experimental results, in terms of I_d , increases. For instance, for $\dot{m}_A = (10, 14)\text{mg/s}$ and $V_s = 450\text{V}$, the mismatch is large, probably suggesting that a non-linear dependence of the turbulent parameters on the operational point is needed. Similarly, when $\dot{m}_A = 8\text{mg/s}$, the results seem to get worse compared to the simulations with constant turbulent parameters. This may suggest that in the fitting law a dependence on \dot{m}_A should be introduced, once more experimental data at these operational points are available. Nevertheless, it must be pointed out that, for nearly all the operational points, simulation performance values are within the

2- σ confidence level of the experimental measurements ($\pm 10\%$).

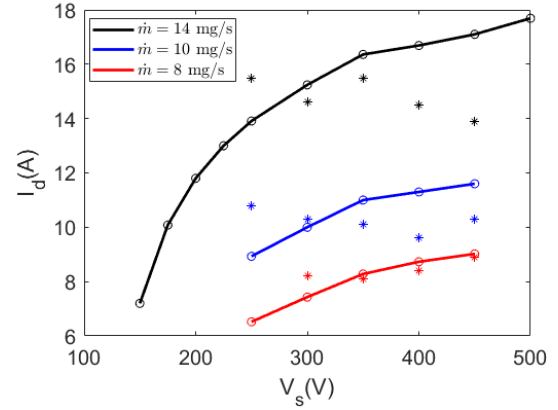


Figure 6: Comparison of numerical (continuous line with circular marker) and experimental results (star markers). The numerical results are obtained using constant α_t for all the operation points.

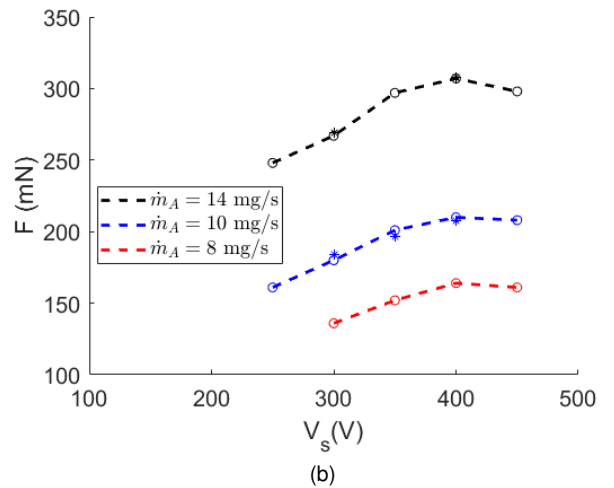
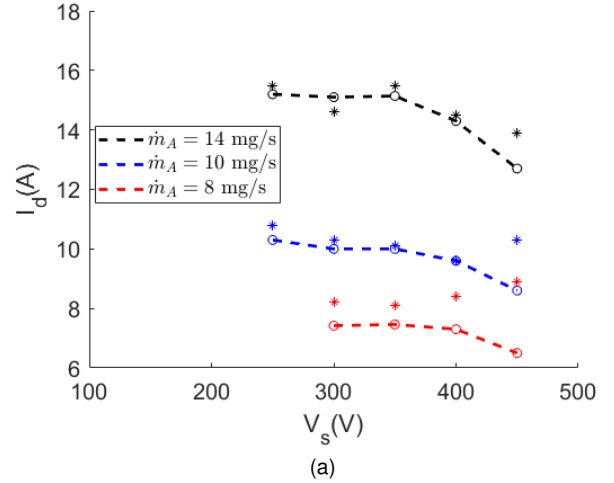


Figure 7: Comparison of numerical (continuous line with circular marker) and experimental results (star markers) of (a) discharge current and (b) thrust.

Table 5: Tuning of the turbulent parameters for different operational points

Op. Point		Constant (α_{t1}, α_{t2}) = (1%, 6%)		Tuned (α_{t1}, α_{t2})		Tuned (α_{t1}, α_{t2})	
\dot{m}_A (mg/s)	V_s (V)	I_d , e%	F, e%	α_{t1}	α_{t2}	I_d , e%	F, e%
10	300	10.0, 3%	180, 2%	1.0	6.0	10.0, 3%	180, 2%
10	350	11.0, 8%	207, 5%	0.9	4.6	10.0, 1%	201, 2%
10	400	11.3, 18%	215, 3%	0.8	3.2	9.6, 0%	210, 1%
14	300	15.1, 3%	266, 1%	1.0	6.0	15.1, 3%	266, 1%
14	400	16.7, 18%	307, 1%	0.8	3.2	14.3, 1%	307, 1%

Table 6: I_d values with and without using the linear fitting for α_{t1} and α_{t2} , obtained from the tuning of these parameters for the operation points in Tab. 5.

Op. Point		Constant	Lin. Fit. (α_{t1}, α_{t2})		Lin. Fit. (α_{t1}, α_{t2})
\dot{m}_A (mg/s)	V_s (V)	(α_{t1}, α_{t2}) = (1%, 6%) I_d , e%	α_{t1}	α_{t2}	I_d , e%
8	300	7.42, 8%	1.0	6.0	7.42, 8%
8	350	8.28, 2%	0.9	4.6	7.46, 8%
8	400	8.73, 4%	0.8	3.2	7.31, 13%
8	450	9.02, 1%	0.7	1.8	6.53, 27%
10	250	8.93, 17%	1.1	7.4	10.3, 5%
10	450	11.6, 13%	0.7	1.8	8.6, 16%
14	250	14.0, 10%	1.1	7.4	15.2, 2%
14	350	16.4, 6%	0.9	4.6	15.14, 2%
14	450	17.2, 24%	0.7	1.8	12.7, 8%

5.4 Current and energy balances and efficiency

The evolution of the performance figures shown in Sec. 5.3 is here further analyzed based on the current and energy balances, and on the values of relevant partial efficiencies. Tab. 7 lists the values of P_d for each operational point together with other important power magnitudes (as percentages of P_d), namely: the energy flow to infinity, P_∞ ; the power loss at the dielectric and anode walls, P_{DW} and P_{AN} , respectively; and the power consumed in inelastic collisions (ionization and excitation), P_{inel} . For a better understanding of each of the power terms, the different boundaries of the simulation domain are depicted in Fig. 3(a). The steady state power balance equation is

$$P_d = P_\infty + P_{DW} + P_{AN} + P_{inel}. \quad (\text{Eq. 6})$$

$P_{z,\infty}$ is a part of P_∞ ; in particular, the flow of axial energy through the free loss boundaries, and therefore considered as a useful power. Then, $P_\infty - P_{z,\infty}$ is considered the non-useful power, or flow of radial energy, lost at infinity. As such, the total power loss, P_{loss} , is considered to be:

$$P_{loss} = P_\infty - P_{z,\infty} + P_{DW} + P_{AN} + P_{inel}. \quad (\text{Eq. 7})$$

Regarding the ion currents, in Tab. 8, we show the ion current generated by ionization in the whole sim-

ulation domain, I_{prod} . Then, expressed as percentages of this magnitude, also Tab. 8 gathers the following important ion currents: the ion beam current or current at infinity, $I_{i\infty}$; and the ion current to the dielectric and the anode walls, I_{DW} and I_{AN} , respectively. These currents fulfill the following balance:

$$I_{prod} = I_{i\infty} + I_{DW} + I_{AN}. \quad (\text{Eq. 8})$$

Then, Tab. 9 gathers a set of partial efficiencies, together with η , for the cases with $\dot{m}_A = 14$ mg/s. These partial efficiencies are the propellant utilization efficiency, η_u ; the production efficiency, η_{prod} ; the current efficiency, η_{cur} ; the charge efficiency, η_{ch} ; the energy efficiency, η_{ene} ; and the divergence efficiency, η_{div} . Their mathematical definitions are:

$$\eta_u = \frac{\dot{m}_{i\infty}}{\dot{m}_A}; \quad \eta_{prod} = \frac{I_{i\infty}}{I_{prod}}; \quad (\text{Eq. 9})$$

$$\eta_{cur} = \frac{I_{i\infty}}{I_d}; \quad \eta_{ch} = \frac{e\dot{m}_{i\infty}}{m_i I_{i\infty}} \quad (\text{Eq. 10})$$

$$\eta_{div} = \frac{P_{z,\infty}}{P_\infty}; \quad \eta_{ene} = \frac{P_\infty}{P_d}. \quad (\text{Eq. 11})$$

The evolution of the partial efficiencies for $\dot{m}_A = 14$ mg/s is shown in Fig. 8. In Fig. 8(a), one can observe that η_u increases with V_s . This means that for the given injected neutral mass flow, the ion mass flow at infinity is larger as the electric energy input

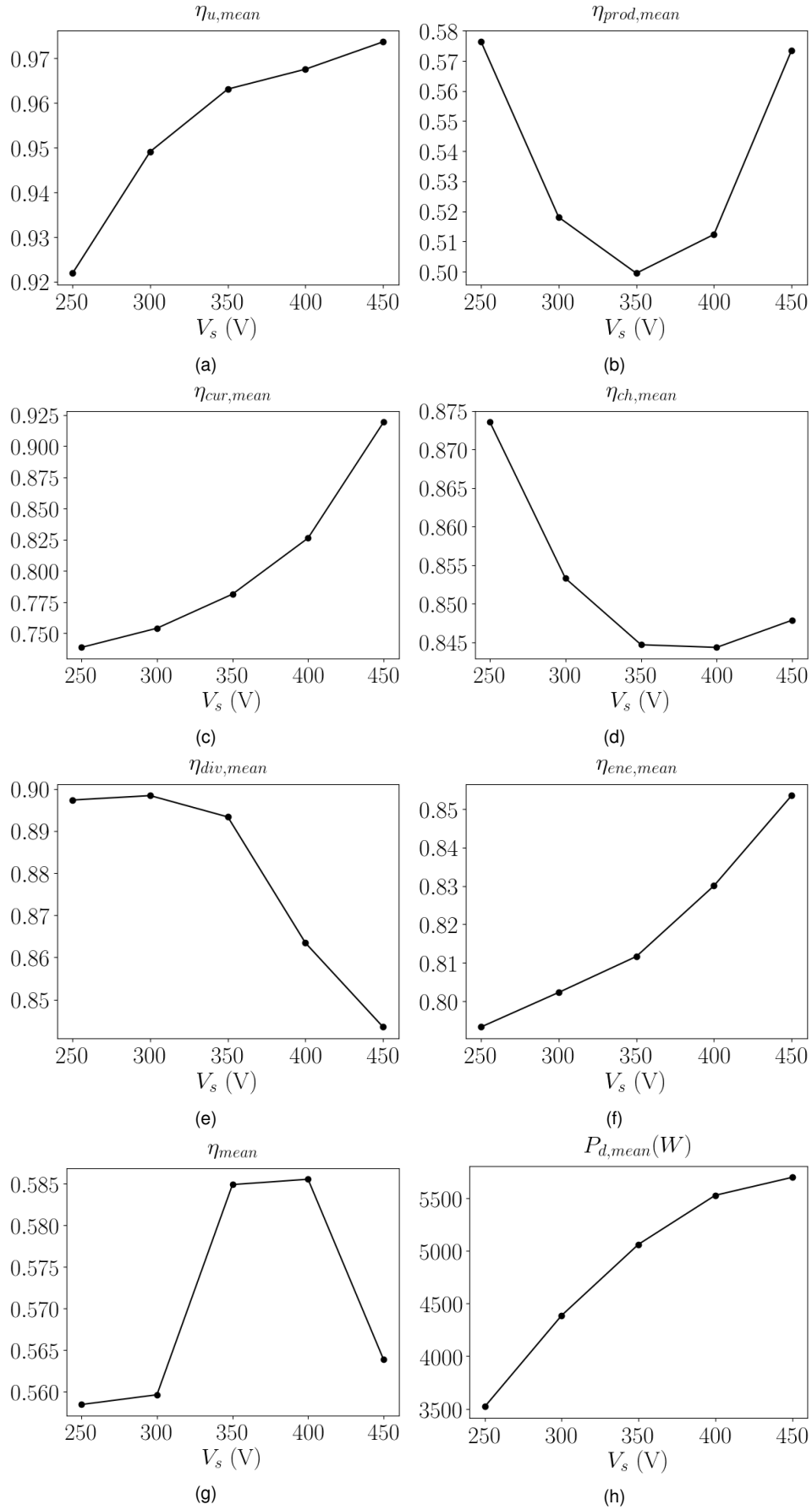


Figure 8: (a)-(g) Time-averaged partial efficiencies, and (h) discharge power, as defined in Eqs. 9 and 10 and 11, for $\dot{m}_A = 14$ mg/s. Their evolution is shown with respect to the source voltage, V_s . The efficiencies are (a) utilization, (b) production, (c) current, (d) charge, (e) divergence (f) energy and (g) thrust efficiencies.

Table 7: Power terms for all the operating points under study. All the terms, except P_d are displayed as percentages of the discharge power.

V_s (V)	\dot{m}_A (mg/s)	P_d (kW)	P_{loss} (%)	$P_\infty - P_{z,\infty}$ (%)	P_{inel} (%)	P_{DW} (%)	P_{AN} (%)
300	8	2.37	30.1	9.4	11.7	4.5	4.5
350	8	2.79	29.6	9.8	10.9	4.7	4.2
400	8	3.11	29.1	10.7	10.0	4.6	3.8
450	8	3.17	26.6	10.4	8.8	4.1	3.3
250	10	2.42	30.1	8.8	12.6	3.9	4.7
300	10	3.05	29.3	9.0	12.1	4.1	4.1
350	10	3.60	28.8	9.3	11.2	4.4	3.9
400	10	3.90	28.9	11.1	10.1	4.2	3.4
450	10	4.00	27.2	11.7	8.8	3.7	2.9
250	14	3.52	28.8	8.1	13.1	3.4	4.1
300	14	4.39	27.9	8.1	12.5	3.6	3.6
350	14	5.06	27.5	8.7	11.5	3.9	3.4
400	14	5.53	28.3	11.3	10.3	3.7	3.0
450	14	5.70	28.0	13.4	8.8	3.3	2.5

Table 8: Current terms for all the operating points under study. All the terms, except I_{prod} are displayed as percentages of I_{prod} . Both the contribution of single and double ion species are taken into account.

V_s (V)	\dot{m}_A (mg/s)	I_{prod} (A)	$I_{i,\infty}$ (%)	I_{DW} (%)	I_{AN} (%)
300	8	12.0	51.8	34.2	14.3
350	8	13.0	49.5	35.3	15.5
400	8	13.3	50.0	34.6	15.5
450	8	12.1	54.2	31.7	14.1
250	10	13.0	57.2	31.0	11.9
300	10	15.4	51.6	34.2	14.3
350	10	16.6	49.5	35.2	15.4
400	10	16.5	50.2	34.5	15.4
450	10	14.9	55.4	31.0	13.5
250	14	18.9	57.6	30.7	11.7
300	14	22.4	51.8	34.1	14.1
350	14	23.5	49.9	35.0	15.0
400	14	23.0	51.2	34.1	14.7
450	14	20.6	57.4	29.8	12.7

to the system increases. This might be due to an increment in the ionization rate. η_u also depends on the level of current losses to the walls, but its evolution is non-monotonic with V_s as evidenced by Fig. 8(b). A maximum of wall losses is observed around 350V, and it is the same for the rest of mass flow cases, as seen in Tab. 8 and Tab. 9.

In Fig. 8(c), η_{cur} is presented. This metric indicates how much of the discharge current, I_d , is used to neutralize the ion beam. The higher is the value of this efficiency, the less input current is lost in producing (by means of ionization) a certain ion beam current. In Fig. 8(c), η_{cur} is observed to monotonically

increase with V_s , probably because an increase of the ionization efficiency. This implies that less I_d is needed to produce a given $I_{i,\infty}$. This could be the reason why, in the performance map analysis, in Fig. 7(a), I_d is observed to decrease with V_s , even when $I_{i,\infty}$ increases in absolute value, as seen in Tab. 8. η_{ch} is depicted in Fig. 8(d). It is constantly decreasing, except for the highest V_s point. This indicates that the production of double ions tends to increase with V_s . Even if it does not vary significantly, it can be another cause for the evolution of η_{cur} . η_{div} , which accounts for the plume divergence losses, also falls with the increment of V_s , as seen in Fig. 8(e). This

Table 9: Partial efficiencies for all the operating points under study. All of them are presented as percentages.

V_s (V)	\dot{m}_A (mg/s)	η_u (%)	η_{prod} (%)	η_{cur} (%)	η_{ch} (%)	η_{div} (%)	η_{ene} (%)	η (%)
300	8	94.8	51.8	82.1	90.0	88.2	79.3	55.4
350	8	97.7	49.5	85.5	89.1	87.8	80.2	59.2
400	8	99.4	50.0	89.9	88.7	86.9	81.7	60.9
450	8	99.5	54.2	99.5	89.0	87.6	83.8	60.0
250	10	91.0	57.2	77.2	90.1	88.8	78.8	54.9
300	10	95.5	51.6	78.8	88.3	88.7	79.7	55.8
350	10	98.0	49.5	81.9	87.4	88.4	80.6	59.3
400	10	98.4	50.2	86.5	87.3	86.5	82.2	59.8
450	10	98.6	55.4	95.7	87.6	86.1	84.5	58.5
250	14	92.3	57.6	73.9	87.4	89.7	79.3	55.8
300	14	95.4	51.8	75.4	85.3	89.8	80.2	56.0
350	14	96.3	49.9	78.1	84.5	89.3	81.2	58.5
400	14	96.6	51.2	82.6	84.4	86.3	83.0	58.6
450	14	97.3	57.4	91.9	84.8	84.4	85.3	56.4

may be due to the fact that with the increase in V_s , together with the axial electric field, the radial electric field becomes more intense. This radial field, which is more important at the channel exit, as seen in Fig. 4 (b), accelerates the ions radially causing divergence losses. Finally, regarding the partial efficiencies, η_{ene} , in Fig. 8(f), has a definition similar to η_{cur} , but in terms of power, instead of current. Thus, their curves are comparable.

In general, it can be concluded that the increase in V_s makes more efficient the production of $I_{i,\infty}$, but at the same time, increases the divergence losses in the plume, which reduce the useful power. The combination of these opposite effects yields a thrust efficiency, η , whose variation is relatively small, as seen in Fig. 8(g). Its combination with the monotonically growing P_d , in Fig. 8(h), according to Eq. 1, causes the growth of F with V_s in Fig. 7(b). Only for the largest V_d point, there is a decrease of F , due to the asymptotic trend of P_d and the sudden small fall of the thrust efficiency, η . These conclusions are valid for the other mass flow cases, as it can be observed in the values of Tabs. 7, 8 and 9.

6 CONCLUSIONS

HYPHEN, a two-dimensional hybrid PIC/fluid HET simulation code, has been used to simulate the magnetically shielded SITAEL HT5k thruster within the frame of the EDDA project. In order to do this, a successful adaptation of HYPHEN code to the simulation of magnetically shielded HET's, featuring complex magnetic topologies, including magnetic singular points, has been done.

HYPHEN electron module uses a turbulent phe-

nomenological model to which the results of the simulations have been proved to be very sensitive. This model features an electron turbulent collisionality with a step-out profile, for which a dependence on the thruster operational point, defined in terms of V_s and \dot{m}_A , has been shown to be required, by means of comparison to experimental results. Therefore, experimental data for a set of 5 operation points are used to improve the electron turbulent model. A linear fitting of the electron turbulent collisionality depending on the input power source voltage is shown to reproduce satisfactorily the thruster experimental I-V curve for a moderate operation range ($V_s = [250-400]$ V, $\dot{m}_A = [10-14]$ mg/s), and nearly all simulation performance metrics lie between the 2- σ confidence interval of the experimental measurements, thus validating the simulation results against experiments. Along the operational points studied, the electron turbulent parameters slightly change with the input power source voltage both in the thruster chamber and near plume region.

In the present work, it has been shown that HYPHEN is capable of providing a sound fully 2D characterization of the plasma discharge of the HT5k thruster, with 2D contour maps of the main plasma properties, including ion and electron streamlines both in the thruster chamber and the near plume region. The magnetic shielding topology seems beneficial from the point of view of erosion, yielding low electron temperatures close to the chamber walls and a main ionization region at the exit of the chamber.

The simulation results indicate that the thrust efficiency does not vary significantly with V_s . Two

opposite effects, when increasing V_s , produce this behavior: a more efficient usage of I_d to produce $I_{i,\infty}$; and less divergence efficiency, this is, larger power losses due to divergence of the beam.

Future work will deal with the extension of the simulated operational map to values of V_s and \dot{m}_A outside the nominal range of operation (i.e. $V_s = 150-250$ and > 500 V). In addition, it is planned to improve the capabilities of the code to be able to simulate the thruster response to dynamic input signals, namely time-varying V_s and \dot{m}_A . This feature can be relevant from a system integration point of view in the frame of the Direct-Drive architecture under development within the context of the EDDA project.

ACKNOWLEDGMENTS

This work has been supported by the EDDA project, funded by the European Union's Horizon 2020 Research and Innovation Programme, under Grant Agreement 870470.

References

- [1] A. Piragino, E. Ferrato, F. Faraji, M. Reza, T. Andreussi, A. Rossodivita, and M. Andrenucci. Experimental characterization of a 5 kW magnetically-shielded Hall thruster. In *Space Propulsion Conference 2018*, SP-2019-427, 2018.
- [2] V. Gianetti, E. Ferrato, A. Piragino, M. Reza, F. Faraji, M. Andrenucci, and T. Andreussi. HT5k thruster unit development history, status and way forward. In *Proc. 36th International Electric Propulsion Conference, Vienna, Austria*, IEPC-2019-878, 2019.
- [3] Adrián Domínguez-Vázquez. *Axisymmetric simulation codes for Hall effect thrusters and plasma plumes*. PhD thesis, Universidad Carlos III de Madrid, Leganés, Spain, 2019.
- [4] Adrián Domínguez-Vázquez, Jiewei Zhou, Pablo Fajardo, and Eduardo Ahedo. Analysis of the plasma discharge in a Hall thruster via a hybrid 2D code. In *36th International Electric Propulsion Conference*, number IEPC-2019-579, Vienna, Austria, 2019. Electric Rocket Propulsion Society.
- [5] G.S. Janes and R.S. Lowder. Anomalous electron diffusion and ion acceleration in a low-density plasma. *Physics of Fluids*, 9(6):1115–1123, 1966.
- [6] A.I. Morozov, Y.V. Esipchuk, A.M. Kapulkin, V.A. Nevrovskii, and V.A. Smirnov. Effect of the magnetic field on a closed-electron-drift accelerator. *Sov. Phys.-Tech. Phys.(Engl. Transl.)* 17: No. 3, 482-7 (Sep 1972), 1972.
- [7] A. Domínguez, D. Pérez-Grande, P. Fajardo, and E. Ahedo. Nomads: Development of a versatile plasma discharge simulation platform for electric propulsion. In *Space Propulsion Conference 2016*, number paper 2016-3124869, Rome, Italy, May 2-6, 2016. Association Aéronautique et Astronautique de France.
- [8] Adrián Domínguez-Vázquez, Filippo Cichocki, Mario Merino, Pablo Fajardo, and Eduardo Ahedo. 2D and 3D hybrid PIC/fluid modelling of electric thruster plumes. In *35th International Electric Propulsion Conference*, number IEPC-2017-209, Atlanta, GA, 2017. Electric Rocket Propulsion Society.
- [9] Filippo Cichocki, Adrián Domínguez-Vázquez, Mario Merino, and Eduardo Ahedo. Hybrid 3D model for the interaction of plasma thruster plumes with nearby objects. *Plasma Sources Science and Technology*, 26(12):125008, 2017.
- [10] Adrián Domínguez-Vázquez, Filippo Cichocki, Mario Merino, Pablo Fajardo, and Eduardo Ahedo. Axisymmetric plasma plume characterization with 2D and 3D particle codes. *Plasma Sources Science and Technology*, 27(10):104009, 2018.
- [11] T. Andreussi, V. Giannetti, A. Leporini, M. M. Saravia, and M. Andrenucci. Influence of the magnetic field configuration on the plasma flow in Hall thrusters. *Plasma Phys. Control. Fusion*, 60(1), 2018.
- [12] T. Andreussi, V. Giannetti, A. Kitaeva, M. Reza, E. Ferrato, L. Onida, A. Leporini, C. A. Paissoni, D. Pedrini, F. Nania, S. Gregucci, and E. Casali. Development status of the xenon propulsion subsystem for the Ital-GovSatCom platform. In *In Proc. 71st International Astronautical Congress, IAC-20,C4,5,5,x59830.*, 2020.
- [13] J.M. Fife. *Hybrid-PIC Modeling and Electrostatic Probe Survey of Hall Thrusters*. PhD thesis, Massachusetts Institute of Technology, 1998.
- [14] F.I. Parra and P.J. Catto. Limitations of gyrokinetics on transport time scales. *Plasma Physics and Controlled Fusion*, 50:065014, 2008.
- [15] D. Pérez-Grande, J. Zhou, A. Domínguez-Vázquez, P. Fajardo, and E. Ahedo. Development updates for a two-dimensional axisymmetric hybrid code for plasma thruster dis-

charges. In *35th International Electric Propulsion Conference*, number IEPC-2017-201, Atlanta, GA, 2017. Electric Rocket Propulsion Society.

- [16] Daniel Pérez-Grande. *Fluid modeling and simulation of the electron population in Hall effect thrusters with complex magnetic topologies*. PhD thesis, Universidad Carlos III de Madrid, Leganés, Spain, 2018.
- [17] R. Santos. *Código híbrido avanzado de motores de plasma de efecto Hall*. PhD thesis, Universidad Politécnica de Madrid (UPM), Madrid, Spain, 2012.
- [18] Diego Escobar. *Electron transport and azimuthal oscillations in Hall thrusters*. PhD thesis, Escuela Técnica Superior de Ingenieros Aeronáuticos, 2015.